ORIGINAL ARTICLE

Laser-induced alloy nanoparticles: Au–Sn thin film morphology influence on the dewetting process

Paulina Dzienny[1] · Tomasz Rerek[2] · Robert Szczęsny[3] · Marek Trzcinski[2] · Łukasz Skowroński[2] · Arkadiusz Antończak[1]

Abstract
In this paper, the impact of thin Au–Sn layers morphology on the formation of laser-induced alloy nanoparticles (ANPs) is investigated. Also, the changes in composition observed over time in thin films are analysed. The influence of deposition rate and elemental composition was studied. The tests were performed on five sets of samples of varying atomic ratios of Au–Sn and film thickness, for which the optical parameters were measured with the spectroscopic ellipsometry technique (SE). The samples were dewetted with a nanosecond Yb:glass fibre laser. All fabricated surfaces were analysed using scanning electron microscopy (SEM). Moreover, the chemical composition of obtained structures was analysed using X-ray photoelectron spectroscopy (XPS) and transmission electron microscopy (TEM).

Keywords Alloy nanoparticles · Laser nanostructuring · Laser-induced dewetting · Intermetallic compounds · Self-organising structures

1 Introduction

It is widely known and well described in the literature that the chemical and physical properties of nanostructures greatly differ from those of bulk materials and this is a consequence of the atomic-scale behaviour of matter: energy quantisation, surface effects, single electron effects, etc. [1, 2]. In bulk materials, properties are an average of all the quantum forces affecting the atoms. Going into nanoscale material reaches the point when the specific behaviour of individual atom molecules dominates, and it can be very different from the state in which they are aggregated. Development in the field of nanotechnology depends mainly on the exploitation of these effects, due to intelligent design of the

shape, size and structure of the nanostructures [3–5]. One of such designs is metallic alloy nanoparticles that inherit properties of the constituent metals. In many cases, the enhancement of, among others, catalytic and optical properties is observed due to the synergistic effects. For example, Au-Pt bimetallic nanoparticles have a hybrid catalytic ability that can be enhanced by light [6]. It all led to a great interest from both academia and industry and, in turn, many applications. To name a few, in catalysis, since alloy nanoparticles exhibit higher catalytic activity than monometallic and their use improves the process [7–9]. Another, in biological imagining, as a drug carriers and therapeutic agents and as potential vaccine adjuvants [3]. Au–Sn nanoparticles are tested in the role of solder, an alternative to traditionally used Sn–Pb alloys [10]. Also, they are applicable in gas sensors—one of the studied ways to enhance the performance of the semiconducting metal oxide nanostructures (SMONs) is their modification with metal nanoparticles and ions [11–13].

The properties of resulting nanostructures can be carefully tailored with the choice of fabrication method and its parameters. One of the techniques that has gained interest is the dewetting of thin films. Such films, up to certain thickness, are generally unstable or metastable in the as-deposited state, poorly wetting the surface. In that state, it is possible for film's internal attractive forces to disrupt the balance and

✉ Paulina Dzienny
paulina.dzienny@pwr.edu.pl

1 Faculty of Electronics, Photonics and Microsystems, Wroclaw University of Science and Technology, Wyb. Wyspianskiego 27, 50-370 Wroclaw, Poland

2 Institute of Mathematics and Physics, Bydgoszcz University of Science and Technology, Kaliskiego 7, 85-796 Bydgoszcz, Poland

3 Faculty of Chemistry, Nicolas Copernicus University in Torun, Gagarina 7, 87-100 Torun, Poland

destabilise the material. As a result, mass transfer occurs and film thickness unevenness is magnified, in turn causing film rupture and its agglomeration into islands/droplets. The process starts at holes (pre-existing or new ones) and at a film edges. The factors that determine the process of dewetting and its results are the film thickness, temperature, the surface self-diffusivity and the energy of the film-substrate interfaces. In non-continuous polycrystalline films, grain size, distribution and grain boundary diffusivities are crucial factors that determine the process's effect [14–17].

Analysing the dewetting process, it is important to consider the substrate as it plays an important factor in structure formation. Both the heat and the radiation not absorbed by layers propagate into them. In dependence on the thermal conductivity, the heat may be dissipated or not, contributing to the temperature of the thin films. Moreover, heated films undergo mechanical stress due to different thermal expansions of the layers and substrate [17]. Also, as mentioned before, the surface energies determine how well the film wets the substrate, on which the dewetting process occurrence depends. An interesting approach to dewetting is the pre-structurisation of substrates in order to achieve precisely controlled arrays of nanodrops [18, 19].

The research on laser-induced dewetting of thin films mainly focuses on single-metal layers, such as Au [20], Ag [21], Ni [22], C [23] and Co [24]. The bimetallic systems examined are Ag-Au [25], Co–Pt [26], Ni-Cu [27], Au–Sn [28, 29], Ag-Pt [30], Rh-Pd [31] and Au-Ni [32, 33], among which the first four references describe laser-induced dewetting. During the traditional, long-time heating additional phenomena occur, such as diffusion of metal particles into the substrate and chemical interactions between metal and substrate. An alternative approach are rapid melting techniques such as ion and electron beams and laser irradiation [14]. The advantages of the latter one are, among others, precise processing down to the micrometre range and the limitation of thermal damage of unprocessed substrate surface, dependent on the thermal diffusion of the material.

During our previous research [28], we observed a correlation between the thin film surface morphology and thickness, and the size and distribution of nanoparticles formed through laser-induced dewetting. Hence, we decided to explore the topic further. This article describes experiments aimed to determine Au–Sn thin layers morphology role in the formation of laser-induced alloy nanoparticles. We analyse the dependence between the deposition ratio of thin films and the resulting grainy structure of the surface, and its consequence on laser dewetting and alloy nanoparticles produced in the process. We also study the changes in thin film structure by adding a thin layer of gold on the bottom that was meant to change the observed grain size. Moreover, we examine the change occurring in thin films over time and its influence on the laser dewetting conditions and resulting nanostructures. To the best of the authors' knowledge, none of the above aspects has been analysed in the literature yet.

2 Materials and methods

2.1 Thin film preparation

As in our previous studies [28], sets of samples with varying sequences of deposition and film thickness (Table 1, Fig. 1) were produced by thermal deposition in a vacuum on the Si(100) wafers from the Institute of Electronic Materials Technology Łukasiewicz—ITME. The purity of the metals used was 99.999% for Sn and 99.997% for Au (Sigma Aldrich). The thin films were deposited at three different rates v_d 0.05, 0.50 and 2.50 Å/s. The deposition rate and the mass thickness of sequentially grown Au and Sn layers were controlled by quartz microbalance. The distance between tungsten basket and substrate was 20 cm and the base pressure was below 2×10^{-5} mbar. Due to diffusion of metals, the resulting thin films do not exhibit clear interfaces
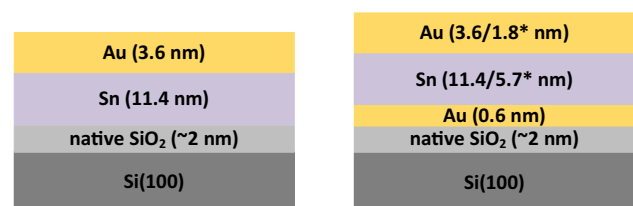

Fig. 1 Schematic representation of the element deposition sequence for E_N, E_S and E_R (on the left) and A_T and A_F* (on the right)

Table 1 Sequence of deposition, thickness, atomic ratio and deposition rate of all examined samples

Sample label	Sequence of deposition	Total thickness h [nm]	Au:Sn ratio	Deposition rate v_d [Å/s]
E_S (S—slow)	Si/Sn (11.4)/Au (3.6)	15	1:2	0.05
E_N (N—normal)	Si/Sn (11.4)/Au (3.6)	15	1:2	0.50
E_R (R—rapid)	Si/Sn (11.4)/Au (3.6)	15	1:2	2.50
A_T (T—thick)	Si/Au (0.6)/Sn (11.4)/Au (3.6)	15.6	1:1.75	0.50
A_F (F—fine)	Si/Au (0.6)/Sn (5.7)/Au (1.8)	8.1	1:1.6	0.50

between gold and tin and are rather a mixture of both elements in the whole volume [34].

2.2 Laser processing

The thin film samples were irradiated using Yb:glass fibre (IPG, YLP series) laser of pulse duration $\tau = 230$ ns and $\lambda = 1062$ nm wavelength. The beam diameter was $2\,\omega_0 = 38$ μm. The samples were prepared by a raster scanning procedure using a galvanometric scanner (Fig. 2). The spot-to-spot distance (d_x) and the hatching distance (d_y) were equal ($d_x = d_y = 100$ μm) and their value was chosen to obtain separate pulses on the surface. The pulse repetition rate $f = 80$ kHz was constant in all irradiation procedures. The parameters were chosen on the basis of previous detailed experiments that resulted in information on the energy range suitable for nanoparticle formation [28].

2.3 Characterisation of samples

2.3.1 Scanning electron microscopy

The surface imagining was conducted using the scanning electron microscopy (SEM). The equipment used was a SEM/Xe-PFIB FEI Helios PFIB microscope with Bruker EDX detector.

2.3.2 Spectroscopic ellipsometry

The spectroscopic ellipsometry (SE) technique was used to examine the optical characteristics of the films. The ellipsometric azimuths (Ψ and Δ) were measured for three angles of incidence (65°, 70° and 75°) in the spectral range of 0.6 to 6.5 eV (191–2066 nm). The ellipsometric measurements were done with the V-VASE instrument from J. A. Woollam Co., Inc.
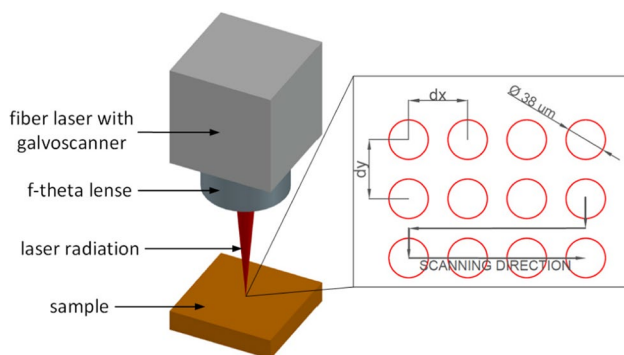

Fig. 2 Schematic representation of the irradiation process

2.3.3 Particle analysis

The ImageJ 1.52v software was used for the particle analysis. The parameters assumed were as in previous research (circularity > 0.5 and area < 1000 nm^2) and all analysis was conducted on the basis of SEM images of 50,000× magnitude, voltage 2.0 kV, current 0.1 nA and 0° tilt angle [28].

2.3.4 X-ray photoelectron spectroscopy

The analysis of the composition and chemical state of the samples was performed using X-ray photoelectron spectroscopy (XPS). The measurements were made in ultra-high vacuum conditions—the base pressure was $2 \cdot 10^{-10}$ mbar. The photoemission process was induced by means of an AlKα X-ray source (1486.6 eV); the angle of incidence of radiation on the surface of the sample was 55° in relation to its normal. Photoelectron energy was recorded with the VG-Scienta R3000 hemispherical analyser. The experimental data after background modelling were fitted to Gauss-Lorentz shapes using the CasaXPS® software. To investigate the composition changes in the subsurface layers, the samples were profiled by etching the surface with an argon ion beam. The ion energy was 4 keV; the incident angle of the ions was 69° with respect to the normal of the samples. The beam scanned a 4×4 mm^2 area of the sample surface to ensure a homogeneous etching of the material. The ion current on the sample surface was approx. 4 μA. The samples were ion-sputtered for a minute periods after which the XPS spectra were recorded.

2.3.5 Transmission electron microscopy

A probe Cs-corrected S/TEM Titan 80–300 FEI microscope, equipped with a Gatan Tridiem 863 spectrometer and Digital Micrograph GATAN ver. 3.43 software, was used to conduct the transmission electron microscopy (TEM) analysis.
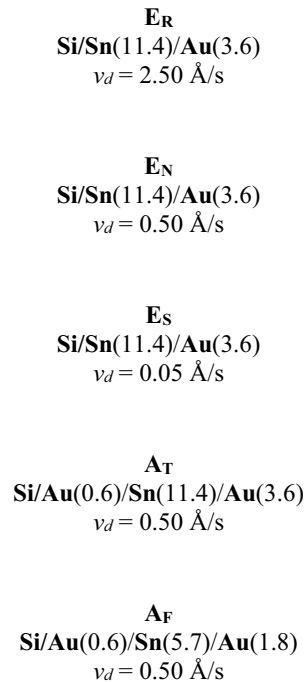
3 Results and discussion

3.1 Characterisation of the samples fabricated by thermal deposition

The SEM images captured under two angles confirmed that the Au–Sn films have a grainy structure (Fig. 3) that differs not only in grain edge shape (visible for 0°) but also height (visible for 52°) and separation.

The varying size of grains in samples is linked to a variety factors. As it was mentioned in our previous study [28], it is the result of the Volmer-Weber growth mechanism that occurs in films produced by thermal evaporation under low vacuum conditions. In it, crystallite seeds are formed in the

Fig. 3 SEM images of all sample surfaces, 0° on the left and 52° tilt on the right; all images in scale

tilt 0° **tilt 52°**

E$_R$
Si/Sn(11.4)/**Au**(3.6)
v_d = 2.50 Å/s

E$_N$
Si/Sn(11.4)/**Au**(3.6)
v_d = 0.50 Å/s

E$_S$
Si/Sn(11.4)/**Au**(3.6)
v_d = 0.05 Å/s

A$_T$
Si/Au(0.6)/**Sn**(11.4)/**Au**(3.6)
v_d = 0.50 Å/s

A$_F$
Si/Au(0.6)/**Sn**(5.7)/**Au**(1.8)
v_d = 0.50 Å/s

first phase, and as the deposited mass increases, the crystallites grow and ultimately (when the layer reaches the necessary thickness) coalesce into a continuous film. In all cases included in this article, the thin layer thickness was lower than the required to obtain a continuous layer.

The difference in microstructure is also associated with the melting point of the deposited metal, which is important in thermal evaporation methods. When the substrate temperature (T_s) is less than 0.1 of the melting point of the metal (T_m)—$T_s/T_m < 0.1$, the resulting layer is composed of extremely small crystallites. Grain growth mainly progresses in orthogonal direction to the substrate. For gold, the melting point is about 1064 °C ($T_m < T_s$), so the resulting layer is formed by very small grains. For tin, $T_m = 232$ °C which means that even at RT the condition of 0.1 $T_m \sim T_s$ is realised, so the grains formed have larger lateral sizes. Furthermore, it should be considered the fact that the substrate is heated due to adsorption of metal vapours and this effect depends (among other things) on the deposition rate. However, in our experiment, the temperature of the substrate could not be controlled during the film deposition.

The order of the applied elements is crucial, since the first layer determines the type of grains—the subsequent layers possibly imitate previous ones. The deposition rate also impacts the morphology of thin films. Higher rates tend to produce larger grains. This fact is related to the proportion T_s/T_m. A higher deposition rate transfers more energy to the substrate in a shorter time, which heats up the substrate (at least temporarily). Consequently, it causes a faster growth

of the crystallites in width, a decrease in the proportion of voids/defects in the formed layer and a decrease in its thickness (not to be confused with mass thickness). In addition, a higher substrate temperature induced by the increase of density of hot metal vapour reaching to the substrate leads to an increase in the efficiency of diffusion processes occurring in the layers.

The E$_N$, E$_R$ and E$_S$ samples were prepared with the same elemental composition, ratio and sequence, but with varying deposition rate, so the last factor decided the differences in morphologies (Fig. 2). As predicted, the lowest deposition rate resulted in the smallest grains.

The A$_T$ and A$_F$ samples were prepared the same way as the E$_N$ one, but with one exception—thin layer ($h = 0.6$ nm) of Au was deposited first, in order to obtain smaller grains (Fig. 2). Also, the A$_F$ sample is significantly thinner ($h = 8.1$ nm in comparison to ~ 15 nm).

3.2 Optical characteristics of prepared samples

Ellipsometric measurements were performed to determine the optical parameters of thin films, such as the linear absorption coefficient α, refractive index n and the extinction coefficient κ (Table 2). The penetration depth δ_p was calculated from the relationship $1/\alpha$.

In all examined cases, the penetration depth values are greater than the thickness of the Au–Sn thin films. This means that a significant part of the energy is absorbed by the silicon substrate, resulting in heating of it and, in

Table 2 The values of the optical parameters of the samples for wavelength 1064 nm

Sample	E_S	E_N	E_R	A_T	A_F
α [nm^{-1}]	0.040	0.042	0.055	0.017	0.005
δ_p (1/α) [nm]	24.8	23.7	18.3	57.8	191.3
n	3.78	3.65	3.37	3.15	2.49
κ	3.40	3.55	4.59	1.46	0.44

consequence, the layers. A significant change is visible for the samples with additional layer of Au—their absorption coefficient is smaller in comparison to other samples, resulting in higher penetration depth. The A_T and A_F samples are built of strongly separated crystallites (large voids between grains uncover the substrate), as can be seen in Fig. 2. The discontinuity of the layers is evident in the optical properties at low photon energies. There is light absorption associated with the interaction of incident light with free electrons, which is described by the Drude model. For samples with additional gold layer, the discontinuity of the Au–Sn film results in the Drude term having a very low amplitude and, consequently, a low light absorption. The effect is stronger in A_F sample due to smaller size of the grains. Similar dependence is visible comparing E_S and E_N samples with E_R—the last one has higher value of the extinction coefficient, due to bigger grains.

3.3 The ageing effects on the deposited thin films

In Au–Sn bilayer systems, gold was on the surface to limit the tin oxidation. The thickness of Au was 3.6 nm (1.8 nm for A_F sample). For layers applied with this method and under these conditions, the gold film is not continuous, also, there is an oxygen diffusion into the layers, so oxidation of tin cannot be avoided. The oxidation process could also change the optical properties of the produced samples. Another factor can be ongoing diffusion of elements between the layers. In order to investigate the changes in sample structures in time, spectroscopic ellipsometry and X-ray photoelectron spectroscopy were used.

Figures 4 and 5 present the refractive index (n) and extinction coefficient (κ) for the fabricated E_N, E_S, E_R, A_T and A_F layers as well as the absorption coefficients α. The reported results of ellipsometric measurements show changes that occur in the optical properties of Au–Sn films with their ageing. This effect is a consequence of changes in morphology of thin films. The sequential method of layer deposition (Sn first, then Au) is not negligible. The boundary of Au and Sn films is characterised by high dynamics, both materials form an alloy and diffusion at their boundary is initiated, already at room temperature, and intermetallic compounds such as AuSn, AuSn$_2$, AuSn$_4$ or Au$_5$Sn are formed [35]. At temperatures much lower than the melting point of the material, grain boundary diffusion is a primary component of diffusion. Consequently, for less extensive surface films composed of small grains, this diffusion should proceed faster. The microstructure of the films obtained by thermal evaporation strongly depends on their deposition conditions (e.g. rate or substrate temperature). This effect has been observed and described in [36] and is visible in the microstructure of the produced films (mainly in E_N, E_S and E_R). The most significant changes in optical properties are observed for the E_R layer, which was fabricated at a much higher rate (2.5 Å/s) than the E_N and E_S samples. For the E_N and E_S films, the changes in optical properties that evolved are at a similar level. The changes in the optical properties of layers A_T and A_F are smaller than in the E-series systems.
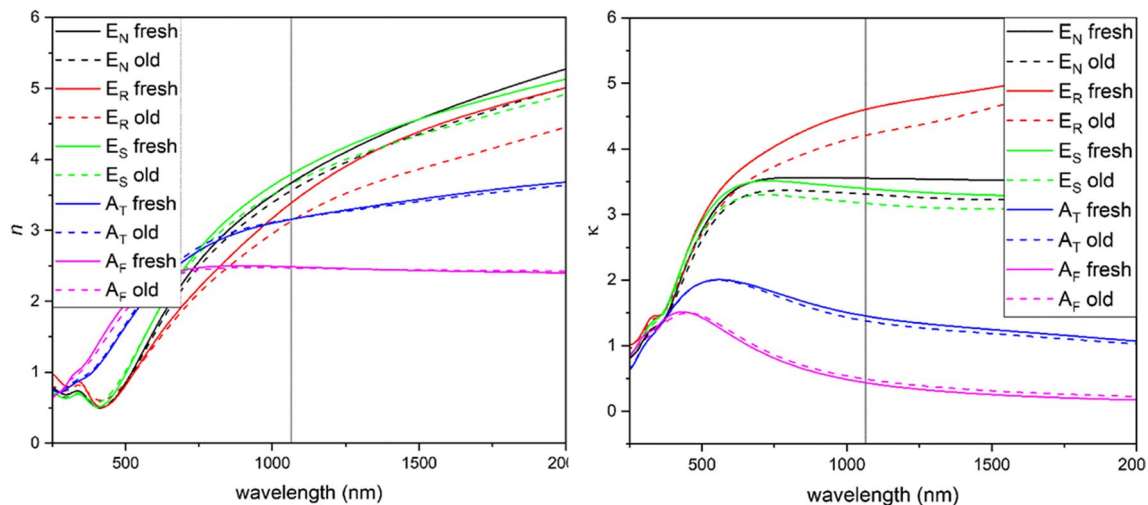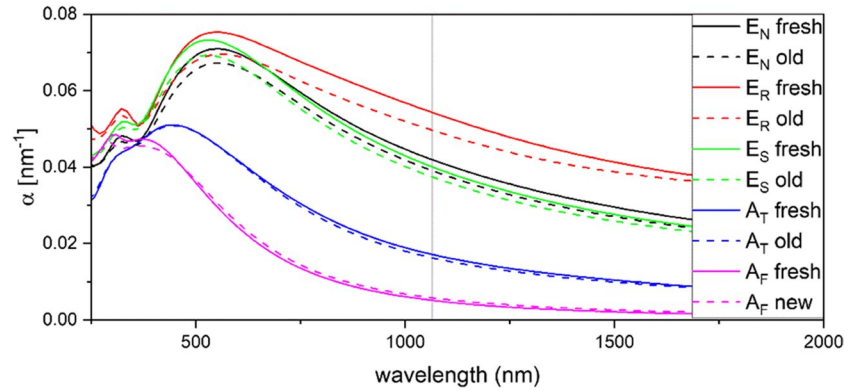

Fig. 4 Refractive index and extinction coefficient spectra for freshly prepared samples and after 3 months; marked 1064 nm

Fig. 5 Absorption coefficient spectra for samples after production and in 3 months after; marked 1064 nm

These structures are different from the previous ones by the fact that a gold film 0.6 nm thick was deposited before the Sn coating. This procedure caused differences in the formation of the layers.

To further investigate, XPS measurements were conducted on fresh and aged samples E_N, both on the surface and subsurface layers—first layer after 1 min of sputtering and second after another minute (Fig. 6).

The Au4f level for all thin films can be fitted with two components (Fig. 6a and b). The energy of the $Au4f_{7/2}$ level ~ 84 eV suggests the content of metallic gold, whereas the energy level ~ 84.8 eV suggests the presence
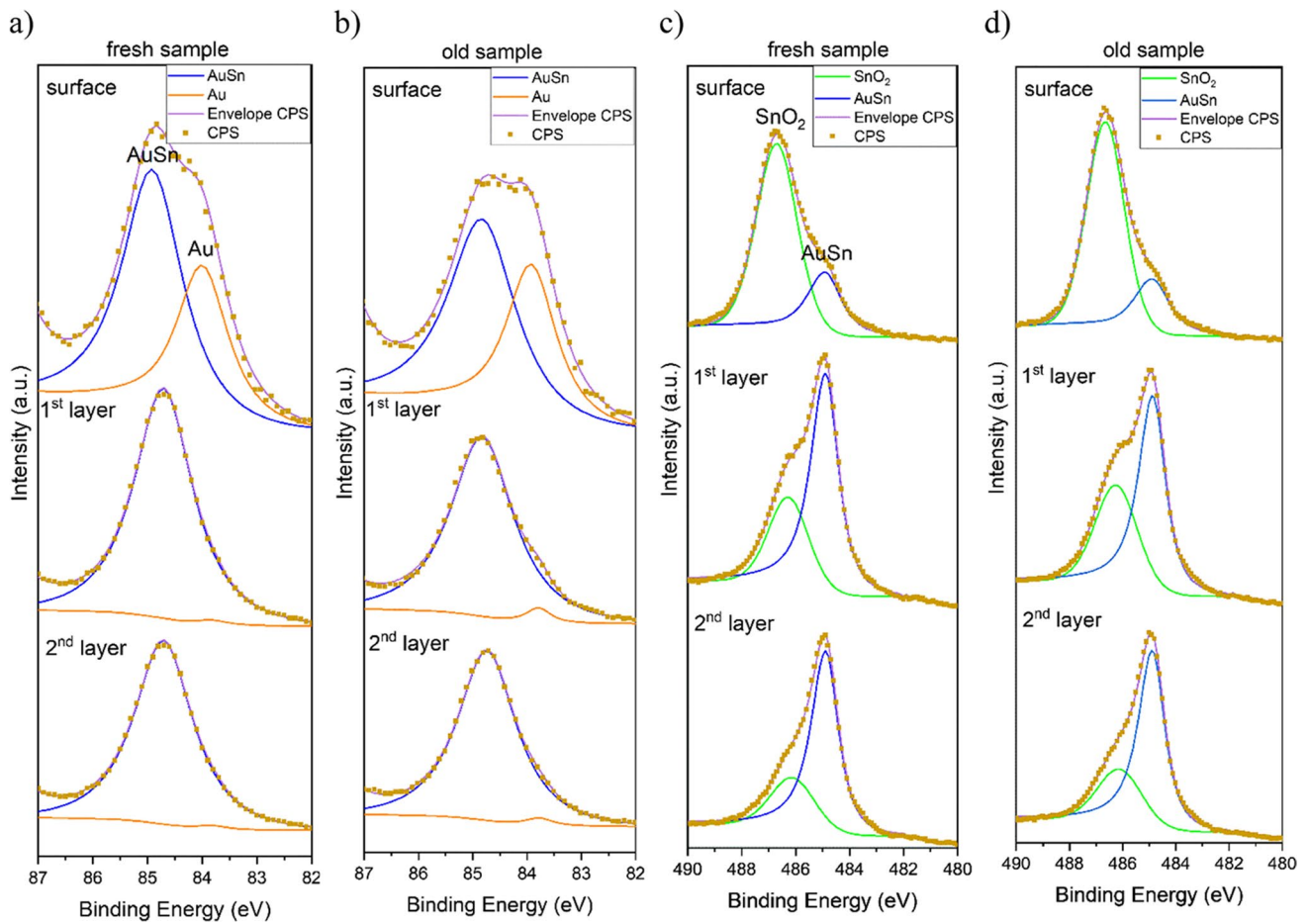
Fig. 6 XPS spectra for samples E_N: **a** $Au4f_{7/2}$ measured 1 week after removal from PVD machine; **b** $Au4f_{7/2}$ measured 3 weeks after removal from PVD machine; **c** $Sn3d_{5/2}$ measured 1 week after removal from PVD machine; **d** $Sn3d_{5/2}$ measured 3 weeks after removal from PVD machine

of AuSn. Below the surface, the intensity of metallic Au peak drops significantly which indicates that below 1 nm of the surface almost all gold is in the form of AuSn. The main distinction between the spectra of fresh and aged samples is in the intensity ratio of the mentioned lines, as the measurements suggest a higher content of AuSn on the surface of fresh samples (Table 3). It indicates that with time, AuSn partially breaks down into Au and Sn.

The $Sn3d_{5/2}$ characteristic presented in Fig. 6c and d can be fitted with two components. The energy level ~ 484.9 eV suggests the presence of AuSn or metallic Sn, while the energy level ~ 486.6 eV suggests the formation of SnO_2. Below the surface, the intensity ratios of the mentioned peaks change—the SnO_2 content drastically falls in favour of AuSn or Sn. The one difference between spectra of fresh and aged samples is in the intensity ratio of mentioned lines—the measurements suggest higher content of SnO_2 on the surface of older samples. It indicates that with time, part of AuSn is converted into SnO_2 and Au, which corresponds with the changes in Au4f spectra described above.

It is reported in the literature that the oxidation of Au–Sn alloys is similar to the oxidation of pure Sn [37]. The described changes may explain the difference in laser radiation energy needed to achieve the same effect on fresh and old samples, described in the next paragraph. This phenomenon may arise from the melting temperature of Au (~ 1064 °C bulk) and SnO_2 (~ 1630 °C). The latter is significantly higher than AuSn (~ 278 °C bulk, varies in dependence on composition). The unmolten tin oxide in liquid metal increases the viscosity of the resulting composite [38].

Table 3 Table of XPS peak height ratios, spectra of surface, after 1 min of sputtering (1st layer) and another 1 min (2nd layer)

	AuSn:Au ratio		AuSn:SnO_2 ratio	
	Fresh sample	Old sample	Fresh sample	Old sample
Surface	1:0.58	1:0.64	1:2.77	1:4.25
1st layer	1:0.03	1:0.03	1:0.45	1:0.63
2nd layer	1:0.01	1:0.02	1:0.34	1:0.39

Fig. 7 The SEM images of structures formed on E_N sample, both images in scale

3.4 Laser-induced dewetting of the Au–Sn thin films

3.4.1 Evolution of nanostructures

The use of laser beam with a Gaussian intensity distribution made it possible to observe the effect of range of energy densities under the single laser pulse. When the radiation energy E does not exceed the minimum value E_D, no changes are visible on the surface. The fully developed structures can be obtained when the energy exceeds the characteristic threshold E_D necessary for the full process ($E > E_D$). When the energy reaches the ablation threshold ($E > E_A$), the surface undergoes removal (not presented in the paper) [28]. During experimentation, it has been noticed that on samples irradiated in some time after removal of the thin films from PVD chamber additional region appeared. In this area, the nanoparticles are not fully formed, what means that the pulse energy was insufficient for the dewetting process to complete, but enough to initiate it ($E_{Dmin} < E < E_D$) (Fig. 7)—the oxide component changes the rheology of molten material and impedes its flow, what causes the necessity of usage of higher energy values for film to fully retract.

The consequence of these changes is the increase of the energy value necessary to obtain fully formed structures. With time passing, higher pulse energy was necessary to cause visible effect on the thin films and to form alloy nanoparticles. In Fig. 8, we present the phenomenon on the chosen example: effects of irradiation of E_R sample in 1 week, 1 and 3 months from removing from PVD chamber. The change in the 15 nm samples was significantly smaller than in ~ 7.5 nm. In case of E_S and E_R samples, the difference between 1 week and 1 month was around 0.5 µJ and another 2 months 0.25 µJ. A significant difference in time necessary for change of dewetting process between the thin films was observed—samples E_R stand out requiring the most time for it to occur. Since it has the biggest and most flat grains among analysed thin films, what equals the lowest surface/volume ratio, it is suspected that the oxidation process is the slowest.

As it was mentioned, in polycrystalline thin films the grain boundaries serve as a source of fluctuation required for the dewetting phenomenon to begin. It is particularly visible
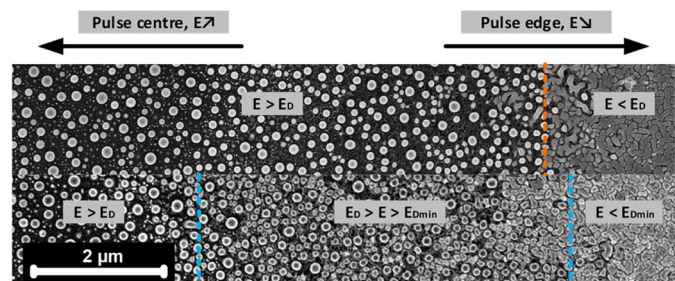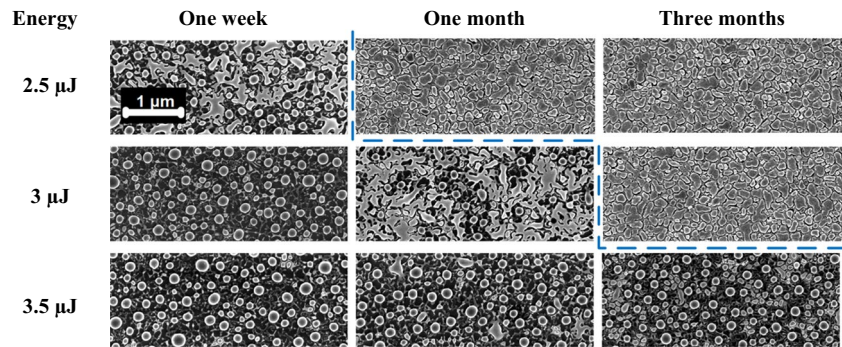

fresh E_N sample

old E_N sample

Fig. 8 The SEM images of structures formed on E_R sample, all images in scale

Energy	One week	One month	Three months
2.5 μJ			
3 μJ			
3.5 μJ			

in case of oxidised samples. The samples irradiated with a range of pulse energies underwent the SEM imagining. In Fig. 9, selected sample images are compiled. The amount of energy is the same for samples in row. Close inspection of images of surfaces with not yet fully developed structures confirms that they originate in grains. Therefore, the average size of the nanostructures is influenced by the average size of the grains. We suspect that this relation will become less direct with the increase of the film thickness, since the size mainly depends on the overall volume of the material. The particle analysis procedure of ImageJ results in information about nanostructure size distribution and the area of the surface covered. Analysing, we can observe that the least amount of nanostructures is observed on E_R sample, the one with the lowest amount of grains. The total sample area covered by the nanostructures is (on average) 28% for E_N and E_S and 15.5% for the E_R sample. For the A_T and A_F samples, the values were 25% and 22%, respectively.

The size range of the nanoparticles was divided into 18 subranges of 10 nm each. The standardised size distributions for chosen samples with well-developed nanostructures can be seen in Fig. 10. Since the distribution for samples with well-developed structures were similar in wide range of parameters, we decided to present as example samples presented in Figs. 8 and 10. Please note that due to the method limitation the lower limit of the nanoparticle sizes was set to 35 nm. The statistics confirm what can be seen on the images. In comparison with E_S, E_R sample shows lesser amount of nanoparticles above 75 nm diameter. Also, their distribution is more even, without the clearly visible mode of size.
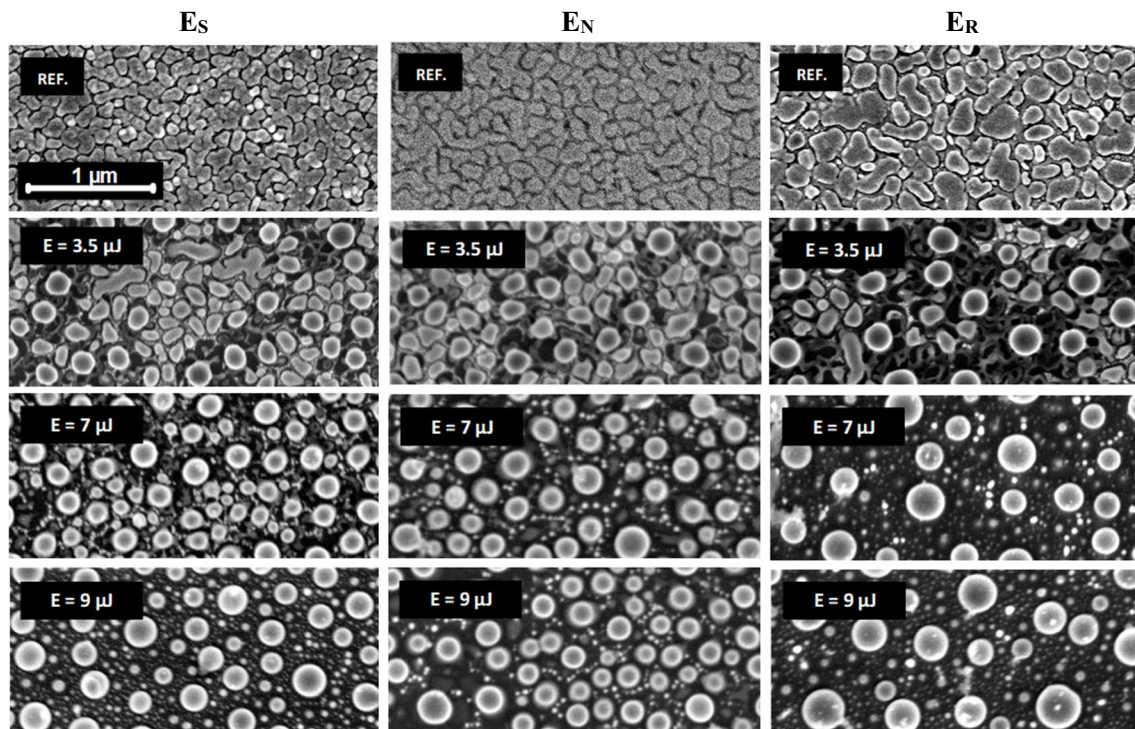

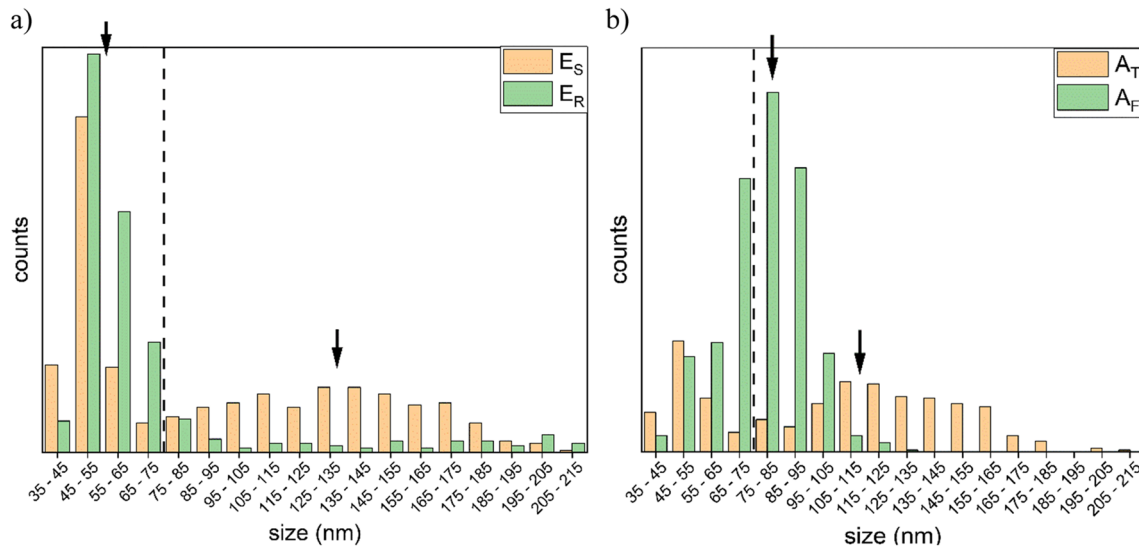**Fig. 9** SEM images of irradiated surfaces, all images in scale

Fig. 10 Size distribution of nanoparticles formed on the **a**) E_S and E_R, **b**) A_T and A_F samples

The distribution shown in Fig. 10b confirms the observations made in previous experiments with the usage of different samples that the medium size of nanostructures strongly depends on the layer thickness—from thinner layers smaller nanostructures are formed (Fig. 11).

The experiments described in our previous work [28] concluded that the final result of the laser dewetting depends on the highest energy deposited on surface per single impulse, not on the accumulated fluence. In case of overlapping impulses in comparison to experiments with single pulses, the amount of energy delivered on the surface necessary to obtain the same surface morphology decreases only slightly and it is probably connected with the Si substrate heating, not the thin layer absorption.

3.4.2 Structural and compositional characterisations of nanostructures

STEM/TEM/EDX measurements were conducted for samples E_R and A_T. In both cases, two sets of particles were visible in the prepared specimens: dominant large structures (100–200 nm for E_R and 60–90 nm for A_T) and small ones (10–20 nm). The first ones were characterised in detail. STEM-EDX analysis indicates an essential difference between A_T and E_R samples which is visualised in Fig. 12.

The results obtained for sample E_R indicated rather uniform Au and Sn atoms distribution within the tested nanostructure. The estimated gold:tin ratio was about 1:1. The analysed nanoparticle from sample A_T pointed to the presence of Sn- or Ag-reach areas and thus on multi-compositional character of the nanoparticle. The most interesting is the bottom part of the particle where the bimetallic particle is laying on the thin padding. This arrangement is well visualised by the insert in Fig. 12b.

The selected area electron diffraction (SAED) of E_R particle consists of sharp single spots and polycrystalline rings which can be connected mainly to AuSn (d-spacing (nm)/plane: 0.378/(100), 0.310/(101), 0.229/(102), 0.210/(110)). The analysis of the high-magnification STEM (Fig. 13a) and TEM images of E_R also pointed lattice distances corresponding to the d-spacing from the AuSn planes. Comparing our results discussed here with those published in 2021 [28], some differences should be mentioned. The sample deposited with a rate of 0.5 Å/s (previous studies) seems to have more multi-phase character. For example, the tin oxide crystalline phase was not detected for E_R (deposition rate 2.5 Å/s). The initial deposition rate has an impact on the morphology of the layer and which also affects ageing (oxidation of layers) and, finally, on the dewetted nanostructure composition. This

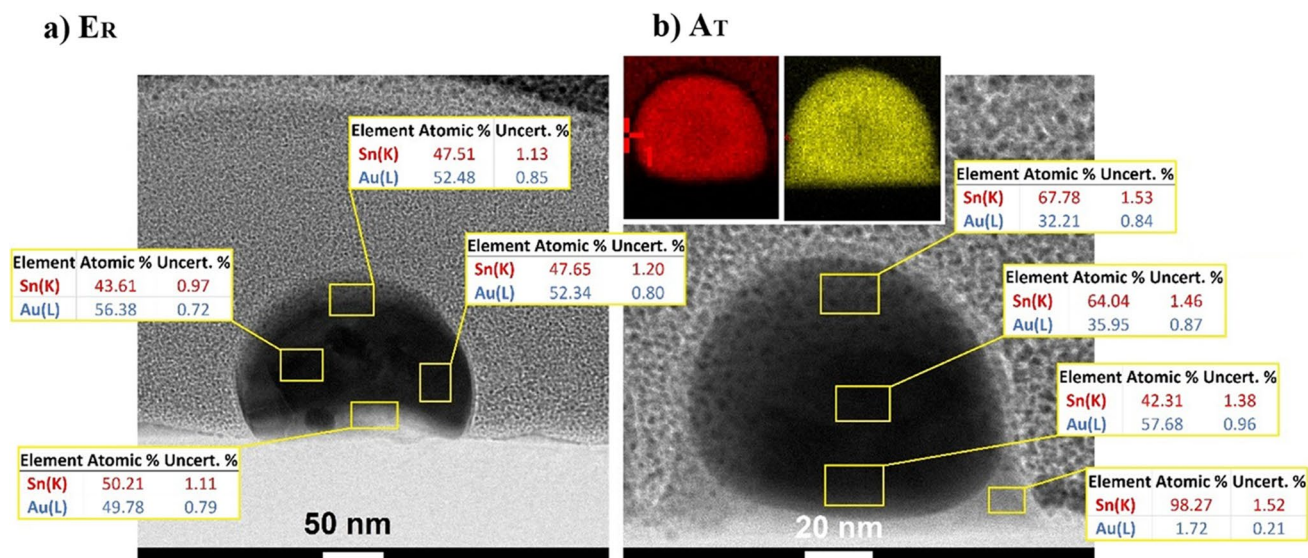**Fig. 11** SEM images of chosen dewetted samples, images in scale

A_T sample, E = 8.5 μJ A_F sample, E = 15 μJ

1 μm
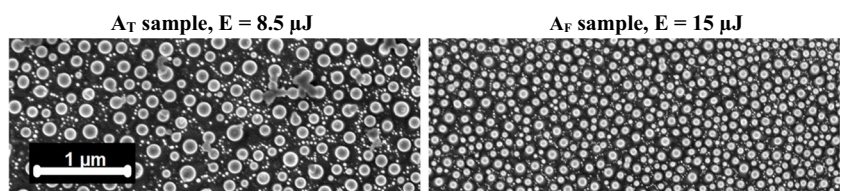
Fig. 12 STEM-EDX analysis of samples E_R (**a**) and A_T (**b**) with estimated Au:Sn ratios for selected areas of nanoparticles. Insert in **b** is the nanoscale element mappings of a single A_T particle

Fig. 13 STEM/TEM analysis: **a** STEM image of A_T particle (scale bar 2 nm) with indicated 0.375 nm d-spacing from AuSn (100) or $AuSn_2$ (112) and **b** TEM image of bimetallic particle (scale bar 10 nm) with TEM lamella (the Pt layer) and Sn-rich area on the bottom of nanoparticle
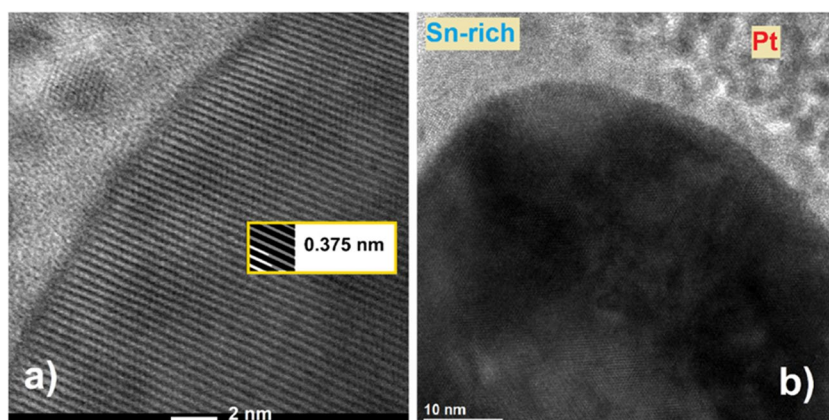
opens the way for controlling the oxide content on the nanoparticles, since potential applications may depend on its presence [39].

The most interesting in the case of the sample with a thin underlayer of gold (A_T) was the formation of a tin "saddle". The detailed investigation of TEM/STEM images of this part of the nanostructure shows its rather amorphous character. The elemental composition indicates that this area consists of 17.95% of tin and 37.32% of oxygen resulting in the Sn:O ratio clearly pointing to SnO_2 formation. The crystalline structure of the At nanoparticle was studied by direct lattice fringes estimation, SAED and FFT images analysis. Some of the d-spacing cannot be unequivocally assigned; however, comprehensive analysis suggests the presence of $AuSn_2$ and AuSn phases. Moreover, the SAED indicated the monocrystalline-like character of this particle.

4 Conclusions

The paper investigated the influence of the morphology of Au–Sn thin films on the laser dewetting process and the morphology of the produced alloy nanoparticles. Two types of films were analysed: (i) series of the same elemental composition and deposition sequence but varying evaporation ratio and (ii) series of the same ratio but additional gold layer on the bottom. The influence of ageing processes occurring in thin layers of substrates on the dewetting process was also determined.

It has been shown that thin films significantly change optical parameters with time from deposition. The degree of these changes depends on the initial morphology and composition of the films. The shift can be attributed to two processes that occur within the deposited samples: the oxidation

of the layers and the diffusion of the elements between and within layers. The analysis of chemical composition (XPS) confirmed the source of mentioned transformations—spectra analysis shown the increase of SnO_2 content on the surface and the breaking down of AuSn into Au and Sn with time.

It has been proven that the recorded changes in the composition of the layers affect both the dewetting process and its final result. The tin oxide content changes the rheology of molten material and impedes it flow. Also, higher laser pulse energy values are necessary for alloy nanoparticles to form from aged samples.

The size of the alloy nanoparticles depends mainly on the thin film thickness, since it decides the volume of material to agglomerate. However, it was shown that in limited range the size and distribution of the NPs may depend on the size of the grains. It occurs in the case of films not thick enough to form a continuous surface. In this paper, thin films of the same composition but slightly different granularity (achieved through changes in growth resulting from different evaporation rate) were compared.

The analysis of the morphology and phase composition (STEM/TEM/EDX) showed multi-phase composition within the single nanoparticle, with mainly AuSn content. The presence of SnO_2 external layer depends on the initial state of the thin films—whether they were covered by native oxide. Also, the NPs produced from oxidised thin films seem to have more multi-phase character, but this dependence needs to be investigated further.

Declarations

Competing interests The authors declare no competing interests.

References

1. Ashby MF, Ferreira PJ, Schodek DL (2009) Nanomaterials, nanotechnologies and design an introduction for engineers and architects. Elsevier Ltd.
2. Binns C (2010) Introduction to nanoscience and nanotechnology. John Wiley & Sons
3. Huynh KH, Pham XH, Kim J, Lee SH, Chang H, Rho WY, Jun BH (2020) Synthesis, properties, and biological applications of metallic alloy nanoparticles. Int J Mol Sci 21:1–29. https://doi.org/10.3390/ijms21145174
4. Cui Z (2008) Nanofabrication: principles, capabilities and limits, 1st edn. Springer, New York
5. Tseng AA (2011) Tip-based nanofabrication, 1st edn. Springer, New York
6. Gilroy KD, Ruditskiy A, Peng H, Qin D, Xia Y (2016) Bimetallic nanocrystals: syntheses, properties, and applications. Chem Rev 116:10414–10472. https://doi.org/10.1021/acs.chemrev.6b00211
7. Kim D, Resasco J, Yu Y, Asiri AM, Yang P (2014) Synergistic geometric and electronic effects for electrochemical reduction of carbon dioxide using gold-copper bimetallic nanoparticles. Nat Commun 5:1–8. https://doi.org/10.1038/ncomms5948
8. Cai Z, Wu Y, Wu Z, Yin L, Weng Z, Zhong Y, Xu W, Sun X, Wang H (2018) Unlocking bifunctional electrocatalytic activity for CO2 reduction reaction by win-win metal–oxide cooperation. AVS Energy Lett 3:2816–2822. https://doi.org/10.1021/acsenergylett.8b01767
9. Kumar B, Brian JP, Atla V, Kumari S, Bertram KA, White RT, Spurgeon JM (2016) New trends in the development of heterogeneous catalysts for electrochemical CO2 reduction. Catal Today 270:19–30. https://doi.org/10.1016/j.cattod.2016.02.006
10. Tabatabaei S, Kumar A, Ardebili H, Loos PJ, Ajayan PM (2012) Synthesis of Au-Sn alloy nanoparticles for lead-free electronics with unique combination of low and high melting temperatures. Microelectron Reliab 52:2685–2689. https://doi.org/10.1016/j.microrel.2012.04.008
11. Li Z, Li H, Wu Z, Wang M, Luo J, Torun H, Hu P, Yang C, Grundmann M, Liu X, Fu Y (2019) Advances in designs and mechanisms of semiconducting metal oxide nanostructures for high-precision gas sensors operated at room temperature. Mater Horizons 6:470–506. https://doi.org/10.1039/c8mh01365a
12. Han Q, Zhang C, Gao W, Han Z, Liu T, Li C, Wang Z, He E, Zheng H (2016) Ag-Au alloy nanoparticles: synthesis and in situ monitoring SERS of plasmonic catalysis. Sensors Actuators, B Chem 231:609–614. https://doi.org/10.1016/j.snb.2016.03.068
13. Yu Y, Dutta P (2011) Examination of Au/SnO2 core-shell architecture nanoparticle for low temperature gas sensing applications. Sensors Actuators B Chem 157:444–449. https://doi.org/10.1016/j.snb.2011.04.088
14. Trice J, Thomas D, Favazza C, Sureshkumar R, Kalyanaraman R (2007) Pulsed-laser-induced dewetting in nanoscopic metal films: theory and experiments. Phys Rev B - Condens Matter Mater Phys 75:1–15. https://doi.org/10.1103/PhysRevB.75.235439
15. Seemann R, Herminghaus S, Jacobs K (2001) Dewetting patterns and molecular forces: a reconciliation. Phys Rev Lett 86:3–6. https://doi.org/10.1103/PhysRevLett.86.5534
16. Leroy F, Borowik Ł, Cheynis F, Almadori Y, Curiotto S, Trautmann M, Barbé JC, Müller P (2016) How to control solid state dewetting: a short review. Surf Sci Rep 71:391–409. https://doi.org/10.1016/j.surfrep.2016.03.002
17. Thompson CV (2012) Solid-state dewetting of thin films. Annu Rev Mater Res 42:399–434. https://doi.org/10.1146/annurev-matsci-070511-155048
18. Ruffino F, Grimaldi MG (2013) Formation of patterned arrays of Au nanoparticles on SiC surface by template confined dewetting

of normal and oblique deposited nanoscale films. Thin Solid Films 536:99–110. https://doi.org/10.1016/j.tsf.2013.03.123

19. Altomare M, Nguyen NT, Schmuki P (2016) Templated dewetting: designing entirely self-organized platforms for photocatalysis. Chem Sci 7:6865–6886. https://doi.org/10.1039/C6SC02555B

20. Ruffino F, Pugliara A, Carria E, Romano L, Bongiorno C, Fisicaro G, La Magna A, Spinella C, Grimaldi MG (2012) Towards a laser fluence dependent nanostructuring of thin Au films on Si by nanosecond laser irradiation. Appl Surf Sci 258:9128–9137. https://doi.org/10.1016/j.apsusc.2011.12.087

21. Krishna H, Sachan R, Strader J, Favazza C, Khenner M, Kalyanaraman R (2010) Thickness-dependent spontaneous dewetting morphology of ultrathin Ag films. Nanotechnology 21:155601–155608. https://doi.org/10.1088/0957-4484/21/15/155601

22. Kwon J, Yoon T, Kim K, Min S, Kwon J, Yoon T, Kim K, Min S (2003) Comparison of the agglomeration behavior of Au and Cu films sputter deposited on silicon dioxide. J Appl Phys 93:3270–3278. https://doi.org/10.1063/1.1556178

23. Felici R, Jeutter NM, Mussi V, Buatier de Mongeot F, Boragno C, Valbusa U, Toma A, Wei Zhang Y, Rau C, Robinson IK (2007) In situ study of the dewetting behavior of Ni-films on oxidized Si (001) by GISAXS. Surf Sci 601:4526–4530. https://doi.org/10.1016/j.susc.2007.04.210

24. Favazza C, Kalyanaraman R, Sureshkumar R (2006) Robust nanopatterning by laser-induced dewetting of metal nanofilms. Nanotechnology 17:4229–4234. https://doi.org/10.1088/0957-4484/17/16/038

25. Oh Y, Lee J, Lee M (2018) Fabrication of Ag-Au bimetallic nanoparticles by laser-induced dewetting of bilayer films. Appl Surf Sci 434:1293–1299. https://doi.org/10.1016/j.apsusc.2017.11.245

26. Oh Y, Kim J, Thompson C V, Ross CA (2013) Templated assembly of Co–Pt nanoparticles via thermal and laser-induced dewetting of bilayer metal film. Nanoscale 5:401–407. https://doi.org/10.1039/c2nr32932h

27. Fowlkes JD, Wu Y, Rack PD (2010) Directed assembly of bimetallic nanoparticles by pulsed-laser-induced dewetting: a unique time and length scale regime. ACS Appl Mater Interfaces 2:2153–2161. https://doi.org/10.1021/am100417x

28. Dzienny P, Szczesny R, Rerek T, Trzcinski M, Skowronski L, Antonczak A (2022) Laser-induced alloy nanoparticles on Au-Sn thin layers. Appl Surf Sci 591:153147. https://doi.org/10.1016/j.apsusc.2022.153147

29. Skowronski L, Trzcinski M, Olszewska A, Szczesny R (2021) Microstructure and optical properties of nanostructural thin films fabricated through oxidation of Au–Sn. Materials (Basel) 14:4034. https://doi.org/10.3390/ma14144034

30. Kunwar S, Pandey P, Pandit S, Sui M, Lee J (2019) Improved morphological and localized surface plasmon resonance (LSPR) properties of fully alloyed bimetallic AgPt and monometallic Pt NPs via the one-step solid-state dewetting (SSD) of the Ag/Pt bilayers. Nanoscale Res Lett 14:1–16. https://doi.org/10.1186/s11671-019-3170-0

31. Abrasonis G, Wintz S, Liedke MO, Akgul FA, Krause M, Kuepper K, Banerjee D, Liu Z, Gemming S (2012) Environment controlled dewetting of Rh–Pd bilayers: a route for core–shell nanostructure synthesis. J Phys Chem C 116:14401–14407

32. Herz A, Wang D, Kups T, Schaaf P, Herz A, Wang D, Kups T, Schaaf P (2014) Solid-state dewetting of Au/Ni bilayers: the effect of alloying on morphology evolution. J Appl Phys 116:044307. https://doi.org/10.1063/1.4891448

33. Wang D, Schaaf P (2012) Ni–Au bi-metallic nanoparticles formed via dewetting. Mater Lett 70:30–33. https://doi.org/10.1016/j.matlet.2011.11.102

34. Rerek T, Skowronski L, Szczesny R, Naparty MK, Derkowska-Zielinska B (2020) The effect of the deposition rate on morphology, opto-electronic properties and formation intermetallic compounds of Au–Sn alloys. J Alloys Compd 849:156041. https://doi.org/10.1016/j.jallcom.2020.156041

35. Tang W, He A, Liu Q, Ivey DG (2008) Room temperature interfacial reactions in electrodeposited Au/Sn couples. Acta Mater 56:5818–5827. https://doi.org/10.1016/j.actamat.2008.08.002

36. Rerek T, Skowronski L, Szczesny R, Naparty MK, Derkowska-Zielinska B (2019) The effect of the deposition rate on microstructural and opto-electronic properties of β-Sn layers. Thin Solid Films 670:86–92. https://doi.org/10.1016/j.tsf.2018.12.009

37. Taylor JA, Merchant SM, Perry DL (1995) Study of the oxidation of gold-tin preforms using X-ray photoelectron spectroscopy. J Appl Phys 78:5356–5361. https://doi.org/10.1063/1.359715

38. Elton ES, Reeve TC, Thornley LE, Joshipura ID, Paul PH, Pascall AJ, Jeffries JR (2020) Dramatic effect of oxide on measured liquid metal rheology. J Rheol (N Y N Y) 64:119–128. https://doi.org/10.1122/1.5117144

39. Chen Y, Kanan MW (2012) Tin oxide dependence of the CO2 reduction efficiency on tin electrodes and enhanced activity for tin/tin oxide thin-film catalysts. J Am Chem Soc 134:1986–1989. https://doi.org/10.1021/ja2108799